

PART IV

Coastal Processes and Sediment Transport



CHAPTER 127

Velocity and Pressure Boundary Conditions for Flow Over the Permeable Boundary of a Porous Medium

İsmail Aydın¹

Abstract

Effect of permeability on pressure distribution over the permeable surface of a porous medium is investigated. Measured pressure distributions comparing impervious and permeable cases are presented. Flow of the free fluid over the permeable boundary and flow of the fluid in the porous medium are computed numerically, maintaining the interaction of the two flow fields through the boundary conditions at the permeable surface. Turbulence is modeled by a low Reynolds number k - ϵ model including a novel technique to model surface roughness effect eliminating the need for wall functions.

Introduction

The interaction between waves, currents and the loose boundary at the sea bottom is a basic question in the study of sediment transport mechanism. In most cases the loose boundary takes an undulated shape with a separating complex flow field on it. The direction and the rate of sediment transport is strongly related to the resulting geometry of the loose boundary and to the dynamics of the flow over the boundary.

Sand particles are removed from the loose boundary by the tangential and the pressure forces, then hold suspended by the vortex structures and carried forward or backward depending on overall flow pattern. In order to define the incipient motion of the sand particles and explain the sediment transport mechanism, a numerical solution of the flow field over the loose boundary is required. However, in such a numerical

¹ Assoc. Professor, Civil Engineering Department, METU, 06531 Ankara, Turkey

solution the boundary conditions for velocity and pressure on a permeable surface should be defined correctly.

Two different flow regions can be defined; flow of the free fluid over the permeable boundary and flow of the fluid within the porous medium of the loose boundary. These two flow fields are strongly interacting. The flow of the free fluid over the undulated surface induces a pressure variation along the common boundary of the two flow regions. This pressure variation and the traction forces acting on the common boundary excite the flow in the porous medium. The velocity, pressure and turbulence along the common boundary are affected by both flow regions.

In flows over a porous medium it is necessary to specify boundary conditions on the tangential and normal components of velocity of the free fluid at the permeable boundary. There exists an extensive analytical literature which describes coupled fluid motions satisfying the Navier-Stokes equations in the free fluid flow and some empirical set of equations in the porous medium with common boundary conditions at the permeable interface of the two flow regions.

Obviously, some uncertainty exists in definition of a true boundary for a permeable material. Therefore, it is useful to define a nominal boundary. In mathematical formulation, a smooth geometric surface is considered to represent the nominal boundary along the surface of the porous medium. The nominal boundary is located at a distance such that the volumetric flowrate between the impervious rough surface and a fictitious surface placed at the tip of roughness elements is equal to the volumetric flowrate between the fictitious surface and the nominal boundary. In numerical computations, hydrodynamic consequences of roughness and permeability are simulated on the nominal boundary.

Experiments

The experiment reported here is designed to examine the nature of the pressure distribution on the nominal boundary of a permeable surface. Briefly, there is a two-dimensional steady flow between an impermeable rippled surface and a flat test surface opposite to the ripple (Fig.1). The ripple geometry is selected to induce a pressure variation on the test surface. Description of the ripple geometry is given in numerical model section. The test surface is either an impermeable flat plate or the permeable boundary of a saturated porous volume.

Three experimental cases are considered. In the first case the test surface is fitted by a smooth solid flat plate. Pressure measurements for this case are indicated as "Impervious" on the figures. In the second case the

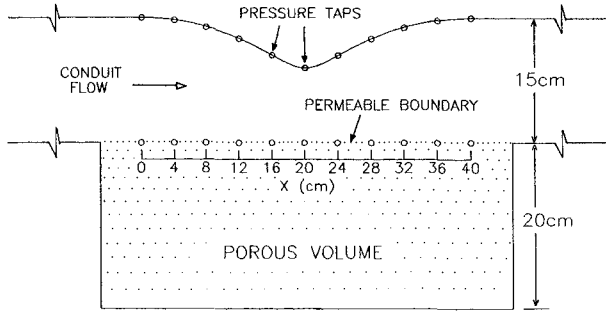


Fig.1 Experimental setup

test surface is fitted by a sieve screen and sand material is placed in the box indicated as "porous volume" in Fig.1. Hydraulic conductivity of the sand is measured to be 1.02 cm/s. Pressure measurements for this case are indicated as "Porous I". In the third case the sand material is replaced with another sample obtained from a different source. Hydraulic conductivity of this material is 1.07 cm/s, almost the same as in the second case. However, particle size distributions of the two sand materials are quite different. Pressure measurements for this case are indicated as "Porous II". The purpose of repeating the experiments with two different sand materials of approximately the same permeability is simply to verify experimental accuracy. Pressure distributions are measured for each case at about 25 different flowrates in the conduit. The maximum (centerline) velocity, U_m , in the conduit is varied between 50 ~ 250 cm/sec.

The measured pressure distributions at the test surface for the impervious and porous cases are shown in Fig.2 for three different flowrates. For $U_m = 95$ cm/s, the difference between the pressures of the three test cases is negligible. Since the velocity is low, neither surface roughness nor permeability can affect the pressure distribution significantly. For $U_m = 159$ cm/s, the pressures for the porous cases are less than the pressure for the impervious case at locations $X \geq 16$ cm along the test surface. This pressure drop is due to the surface roughness effect of the sand material. When the flowrate is increased to $U_m = 248$ cm/s the effect of surface roughness and permeability cancel each other and the resultant pressure distributions for the permeable cases are almost the same as the impervious case pressure distribution. At this high flowrate there is a larger pressure drop due to surface roughness effect of the permeable test surface but, permeability allowing flow into the porous medium from high pressure points and flow out of the porous medium from low pressure points, creates a counter effect to the contraction of flow section by the ripple on the

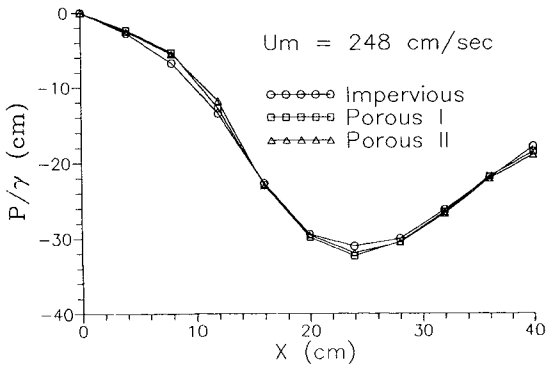
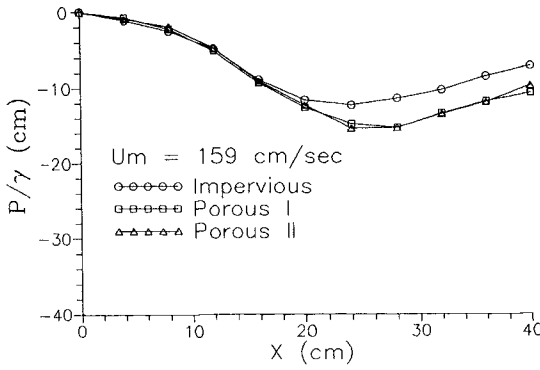
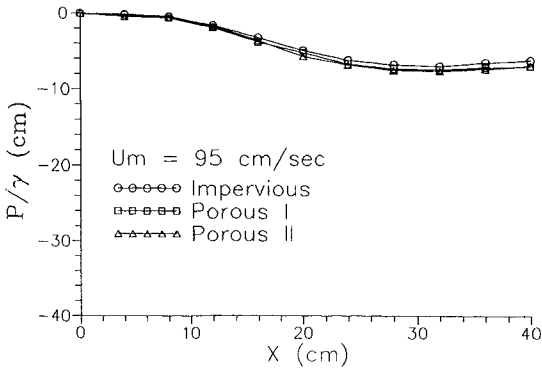


Fig.2 Comparison of pressure distributions along the test surface for flowrates $U_m=95$, $U_m=159$, and $U_m=248$ cm/s.

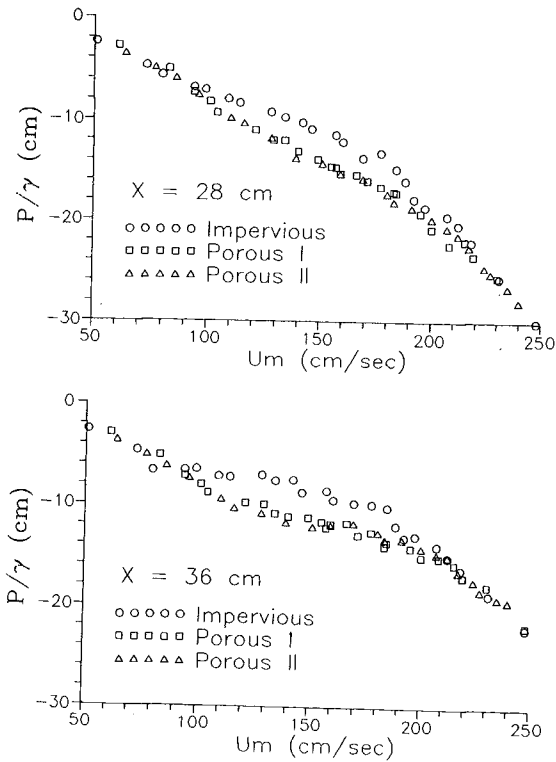


Fig.3 Comparison of pressures at fixed points $X=28$ and $X=36$ cm on the test surface as a function of flowrate in the conduit.

opposite side. In this way the pressure drop due to roughness effect is compensated by the relaxation introduced by permeability of the test surface.

This behavior can better be observed in Fig.3 where pressures at fixed points ($x = 28$, $x = 36$ cm) are compared as a function of flowrate. Pressure drop due to surface roughness can be recognized for $U_m \geq 95$ cm/s and it is compensated by relaxation due to permeability for $U_m \geq 190$ cm/s.

Numerical Model

The flow of free fluid over the permeable boundary and the flow within the porous medium are solved simultaneously allowing interaction of the flow regions through the boundary conditions at the common boundary. Darcy law is assumed to govern the flow in the porous medium. The full

Navier-Stokes equations are solved in the region of free fluid flow and Laplace equation for pressure is solved in the porous medium.

A useful computational grid for the free fluid region is obtained from a conformal mapping between the physical plane (x, y) and the computational plane (ξ, η) defined by Eqns. (1) and (2)

$$x = \xi + c_m \frac{H}{2} \left[\sin \alpha (\xi - \xi_1) e^{\alpha(\eta - \eta_1)} - \sin \alpha (\xi - \xi_2) e^{-\alpha(\eta - \eta_2)} \right] \quad (1)$$

$$y = \eta - \eta_1 - \eta_2 + c_m \frac{H}{2} \left[\cos \alpha (\xi - \xi_1) e^{\alpha(\eta - \eta_1)} + \cos \alpha (\xi - \xi_2) e^{-\alpha(\eta - \eta_2)} \right] \quad (2)$$

$$\text{for } 0 \leq \xi \leq L, \quad 0 \leq \eta \leq \eta_1$$

where $\alpha = 2\pi/L$, $L = 40$ cm, $H = 6$ cm, $\eta_1 = -\eta_2 = 12$ cm, $\xi_1 = 0$, $\xi_2 = L/2$ and $c_m = 1.023598$. For $\eta = \eta_1$ in Eqns. (1) and (2) the ripple geometry used in the experimental setup is obtained. The complete set of governing equations for the free fluid region in the computational plane are written as

$$\begin{aligned} \frac{1}{J} \frac{\partial u}{\partial t} + u_c \frac{\partial u}{\partial \xi} + v_c \frac{\partial u}{\partial \eta} = \frac{\partial y}{\partial \xi} \frac{\partial \bar{P}}{\partial \eta} - \frac{\partial y}{\partial \eta} \frac{\partial \bar{P}}{\partial \xi} + \frac{\partial}{\partial \xi} \left(\nu_c \frac{\partial u}{\partial \xi} \right) + \frac{\partial}{\partial \eta} \left(\nu_c \frac{\partial u}{\partial \eta} \right) \\ + \frac{\partial \nu_t}{\partial \eta} \frac{\partial v}{\partial \xi} - \frac{\partial \nu_t}{\partial \xi} \frac{\partial v}{\partial \eta} \end{aligned} \quad (3)$$

$$\begin{aligned} \frac{1}{J} \frac{\partial v}{\partial t} + u_c \frac{\partial v}{\partial \xi} + v_c \frac{\partial v}{\partial \eta} = \frac{\partial x}{\partial \eta} \frac{\partial \bar{P}}{\partial \xi} - \frac{\partial x}{\partial \xi} \frac{\partial \bar{P}}{\partial \eta} + \frac{\partial}{\partial \xi} \left(\nu_c \frac{\partial v}{\partial \xi} \right) + \frac{\partial}{\partial \eta} \left(\nu_c \frac{\partial v}{\partial \eta} \right) \\ + \frac{\partial \nu_t}{\partial \xi} \frac{\partial u}{\partial \eta} - \frac{\partial \nu_t}{\partial \eta} \frac{\partial u}{\partial \xi} \end{aligned} \quad (4)$$

$$\frac{\partial^2 \psi}{\partial \xi^2} + \frac{\partial^2 \psi}{\partial \eta^2} = - \left[\left(\frac{\partial y}{\partial \eta} \frac{\partial v}{\partial \xi} - \frac{\partial y}{\partial \xi} \frac{\partial v}{\partial \eta} \right) - \left(\frac{\partial x}{\partial \xi} \frac{\partial u}{\partial \eta} - \frac{\partial x}{\partial \eta} \frac{\partial u}{\partial \xi} \right) \right] \quad (5)$$

$$\frac{\partial^2 \mathbf{P}}{\partial \xi^2} + \frac{\partial^2 \mathbf{P}}{\partial \eta^2} = -2\rho \mathbf{J} \left[\left(\frac{\partial v}{\partial \xi} \frac{\partial y}{\partial \eta} - \frac{\partial v}{\partial \eta} \frac{\partial y}{\partial \xi} \right) \left(\frac{\partial u}{\partial \eta} \frac{\partial x}{\partial \xi} - \frac{\partial u}{\partial \xi} \frac{\partial x}{\partial \eta} \right) + \left(\frac{\partial u}{\partial \xi} \frac{\partial y}{\partial \eta} - \frac{\partial u}{\partial \eta} \frac{\partial y}{\partial \xi} \right)^2 \right] \quad (6)$$

where

$$\bar{\mathbf{P}} = \frac{\mathbf{P}}{\rho} + \frac{2}{3} \mathbf{k}, \quad \mathbf{u}_e = \mathbf{u} \frac{\partial y}{\partial \eta} - \mathbf{v} \frac{\partial x}{\partial \eta}, \quad \mathbf{v}_e = \mathbf{v} \frac{\partial x}{\partial \xi} - \mathbf{u} \frac{\partial y}{\partial \xi}, \quad \mathbf{v}_t = \mathbf{v} + \mathbf{v}_t,$$

$$\mathbf{u} = \mathbf{J} \left(\frac{\partial x}{\partial \xi} \frac{\partial \psi}{\partial \eta} - \frac{\partial x}{\partial \eta} \frac{\partial \psi}{\partial \xi} \right), \quad \mathbf{v} = \mathbf{J} \left(\frac{\partial y}{\partial \xi} \frac{\partial \psi}{\partial \eta} - \frac{\partial y}{\partial \eta} \frac{\partial \psi}{\partial \xi} \right),$$

\mathbf{J} is Jacobian of coordinate transformation, \mathbf{v}_t is turbulent viscosity and \mathbf{k} is turbulent kinetic energy. In the porous medium the Laplace equation for pressure is written as

$$\frac{\partial^2 (\mathbf{P}/\gamma)}{\partial x^2} + \frac{\partial^2 (\mathbf{P}/\gamma)}{\partial y^2} = 0 \quad (7)$$

Pressures along the permeable boundary are obtained by integration of the momentum equations on the free fluid side and are supplied as boundary conditions of equation (7) for the potential flow in the porous medium. After solution of the Laplace equation for pressure, the velocity components due to porous media flow are computed. Tangential velocity on the permeable boundary is assumed to have two components. First component is the velocity induced due to the external tangential stress by the free fluid (Beavers and Joseph 1967, Saffman 1971, Taylor 1971) and the second is the velocity of porous media flow due to tangential pressure gradient. These two velocity components are combined to give the "slip velocity" at the permeable boundary.

$$\mathbf{u}_s = -\mathbf{K} \frac{\partial (\mathbf{P}/\gamma)}{\partial x} + c_s \sqrt{\mathbf{K}\mu/\gamma} \left(\frac{\partial \mathbf{u}}{\partial y} \right)_{y=0} \quad (8)$$

where \mathbf{K} is hydraulic conductivity and c_s is the slip velocity coefficient. In the literature slip velocity coefficient may take values between 0.1 ~ 4. In this study it is fixed as unity since the slip velocity has showed no control on the pressure distribution over the permeable boundary for the complete range of

values reported in the literature. The normal component of velocity is simply due to porous media flow and is named as the "seepage velocity" given by.

$$v_s = -K \frac{\partial(P/\gamma)}{\partial y} \quad (9)$$

The slip and seepage velocities are used as the boundary conditions for the momentum equations governing the free fluid flow.

In numerical computation of the free fluid flow a different technique is adopted. In Poisson equation for pressure (Eqn.6) divergence of velocity is not included, instead, the Poisson equation for the stream function (Eqn.5) is solved and velocities are recomputed from the stream function to enforce the continuity after solution of the momentum equations. Otherwise computations were not converging because of the added degree of freedom by the slip and seepage velocities at the permeable boundary.

Turbulent viscosity is obtained from a low Reynolds number $k-\varepsilon$ model as described in (Aydın and Shuto 1988). This model allows a complete numerical solution starting from the boundary, eliminating the need for wall functions. When the wall functions are removed, a new model for the surface roughness is required. This is accomplished by introducing and additional viscosity due to surface roughness (Aydın, 1993). Roughness viscosity is defined in terms of a roughness length scale and the velocity gradient at the wall,

$$\nu_r = l_r^2 \left| \left(\frac{\partial u}{\partial y} \right)_{y=0} \right| \quad (10)$$

and the roughness length scale is given as

$$l_r = 0.4k_s f_r \quad (11)$$

where k_s is the equivalent sand roughness height and f_r is a function to express the turbulence level in terms of the roughness Reynolds number.

$$f_r = \frac{0.1}{\left[1 - \exp(-0.09R_k^{0.6}) \right]} \quad (12)$$

and

$$R_k = \frac{k_s u_*}{\nu} \quad (13)$$

In computations, turbulent viscosity at a point next to a boundary is equated to the roughness viscosity if $\nu_t < \nu_r$.

Computations and Results

Pressure distributions for the first experimental case, the impervious boundary, are computed by the numerical model described above. Computed pressures are compared to experimental data at four different flowrates in Fig.4. In general computation and experiment agrees well, except the end points ($X = 40$ cm). This is due to the uniform flow conditions imposed at the end of the computational domain which may be achieved at further downstream locations. Before computing the permeable cases, effects of surface roughness and permeability are studied separately. Pressure distributions on the test surface for $U_m = 248$ cm/s using different k_s values are shown in Fig. 5. This figure indicates that the pressure drop along the test surface increases with the surface roughness. Fig. 6 shows pressure distributions for the same flowrate using different hydraulic conductivity values keeping $k_s = 0$. It is clearly observed that the increase in permeability reduces the pressure drop on the test surface.

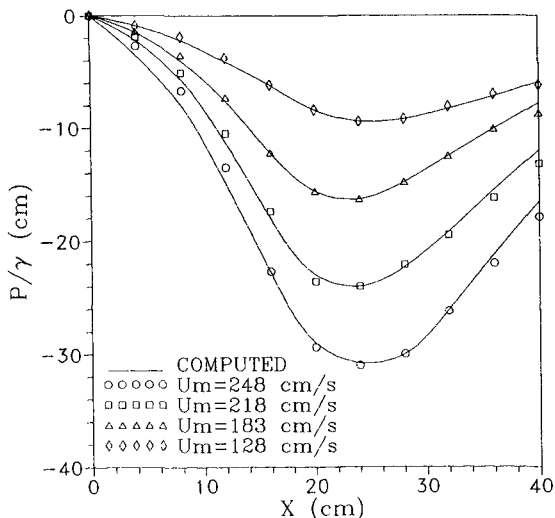


Fig.4 Comparison of computed and measured pressures along the test surface for impervious boundary.

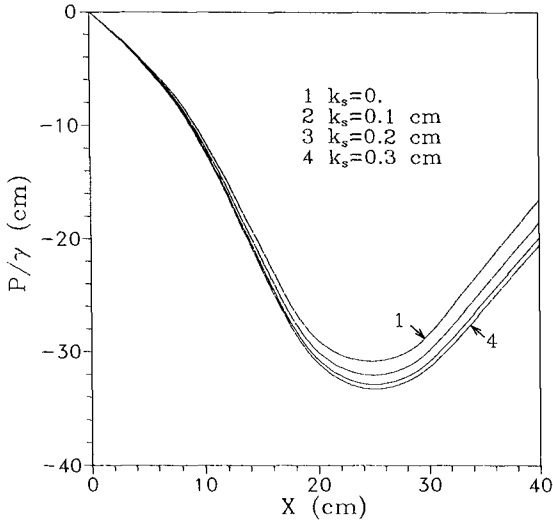


Fig.5 Pressure distributions along the test surface for different surface roughness values.

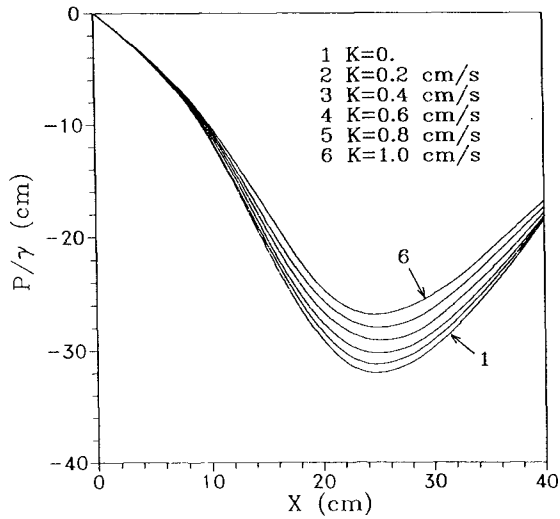


Fig.6 Pressure distributions along the test surface for different hydraulic conductivity values.

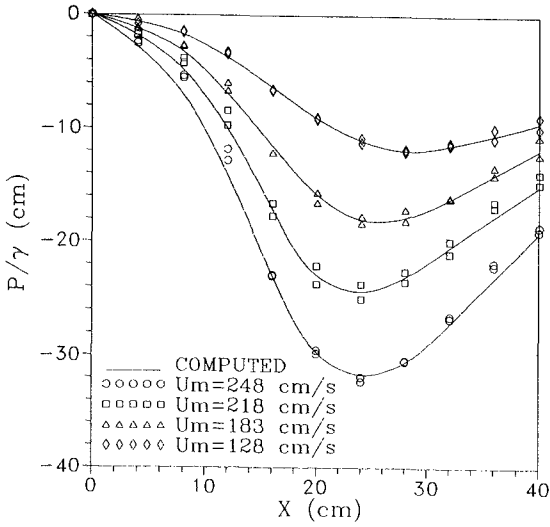


Fig.7 Comparison of computed and measured pressures along the test surface for permeable cases

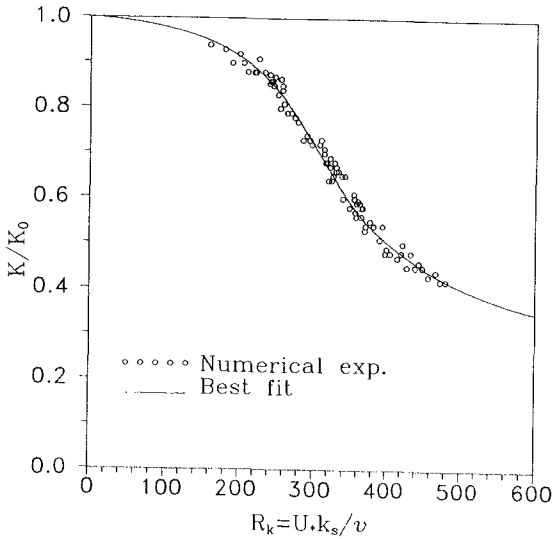


Fig.8 Hydraulic conductivity as a function of roughness Reynolds number along the test surface

The roughness model used in this study, as well as other models, represents the roughness effect due to surface irregularities. When the surface is permeable, the roughness effect will be increased by permeability since it allows turbulent fluctuations to enter into pores of the medium. On the other hand high turbulence due to free fluid flow near the boundary reduces permeability of the surface.

In this study the effect of permeability on roughness effect is ignored and dependence of permeability of a porous boundary to the turbulence level is investigated. Numerical model is forced to satisfy the experimentally measured pressures along the test surface for variable hydraulic conductivity at each computational node. Fig.7 shows a comparison of the measured and computed pressures for permeable test surface with variable hydraulic conductivity. Hydraulic conductivity values used to fit the measured pressures are shown in Fig.8 as a function of roughness Reynolds number. In this figure K_0 represents the hydraulic conductivity for laminar flow conditions. As seen from the figure, hydraulic conductivity is reduced by turbulence when the hydrodynamically rough condition is reached and the reduction is about 50 % at a roughness Reynolds number of 400. However, in order to be able to give an expression of the relation between hydraulic conductivity and roughness Reynolds number, the effect of permeability on surface roughness should be clarified.

Acknowledgement

The publication of the present paper is financially supported by the Ogawa Commemoration Fund of Japan.

References

- Aydin, I. Shuto, N. (1988) An Application of k- ϵ Model to Oscillatory Boundary Layers. **Coastal Eng. in Japan, Vol. 30, No. 2**, pp. 11-24.
- Aydin, I. (1993) Simulation of Rough Surfaces in Turbulent Flow Computation. **Proc. of 1st National Conf. on Computational Mechanics, Istanbul**, pp. 57-56.
- Beavers, G. S. and Joseph, D. D. (1967) Boundary Conditions at a Naturally Permeable Wall, **J. Fluid Mech., Vol. 30, part 1**, pp. 197-207.
- Saffman, P. G. (1971) On the Boundary Condition at the Surface of a Porous Medium. **Studies in Applied Mech., Vol. 1. No. 2**, pp 93-101.
- Taylor, G. I. (1971) A Model for the Boundary Condition of a Porous Material. Part I. **J. of Fluid Mech., Vol. 49, part 2**, pp. 319-326.